Nature and behavior of dislocations in ice

Takeo Hondoh

Institute of Low Temperature Science, Hokkaido University, N19W8, Sapporo 060-0819, JAPAN

Abstract: To better understand various phenomena related to ice-core records, the properties of lattice defects in ice, particularly dislocations, are reviewed. The plasticity of ice significantly affects ice sheet dynamics and ice-core dating. It is well known that ice is predominantly deformed by the basal slip system $<11\bar{2}0>/(0001)$: all nonbasal slip systems are inactive. In particular, the slip systems observed until now are not responsible for uniaxial deformation parallel to the c-axis. However, in spite of difficulties in the nonbasal slip systems, the velocities of dislocations moving on nonbasal planes $<11\bar{2}0>/\{10\bar{1}0\}$ or $<11\bar{2}0>/\{10\bar{1}1\}$ are larger than those on the basal plane. Possible mechanisms for the non-basal slips are discussed in light of recent studies of dislocations in ice. The peculiar nature of ice plasticity is explained by characteristic structures of dislocations in ice, which are responsible for this crystallographic anisotropy.

Dislocations in ice are stabilized by dissociation into two partial dislocations owing to the very low energy of stacking faults lying on the basal plane. Therefore, dislocations in ice have a ribbon-like structure extended on the basal plane so that dislocation motion in ice is restricted to the basal planes. Because of this dissociation, only short segments of dislocations can exist on the nonbasal planes. All possible configurations of dislocations responsible for the nonbasal slip systems are presented. These nonbasal slip systems must operate on a microscopic scale to accommodate stress concentrations caused by deformation, but there is little deformation of the whole specimen.

1. Introduction

On a macroscopic scale, ice is deformed only by the basal slip system; all other slip systems contribute much less to ice deformation. The plasticity of ice is characterized by this strong anisotropy. There is not a large anisotropy in the bond-strengths because water molecules in ice have four neighboring water molecules in a tetrahedral arrangement with almost the same bond length. Instead, the strong anisotropy of plasticity can be understood only through a peculiar property of dislocations in ice that has been investigated during the past two decades. Unless otherwise stated, ice I_h is assumed in the present paper.

A major process for plastic deformation of a crystal is the glide motion

Physics of Ice Core Records
Edited by T. Hondoh
Hokkaido University Press, 2000, Sapporo

of dislocations, which is defined by the motion on a plane (glide plane) parallel to both the Burgers vector and the dislocation line (see Fig. 1(a)). This type of dislocation motion is associated with motions of atoms over very short distances; thus it is much faster than other processes related to mass transport. In comparison, the crystal in Fig. 1(b) deforms also by a climb motion of dislocations, which is defined as motion normal to the glide plane. Because this type of dislocation motion requires absorption or emission of point defects far from the dislocation, it is a relatively slow mechanism of deformation.

Although dislocations are line defects, they can be extended into ribbon-like structures on a plane associated with a low-

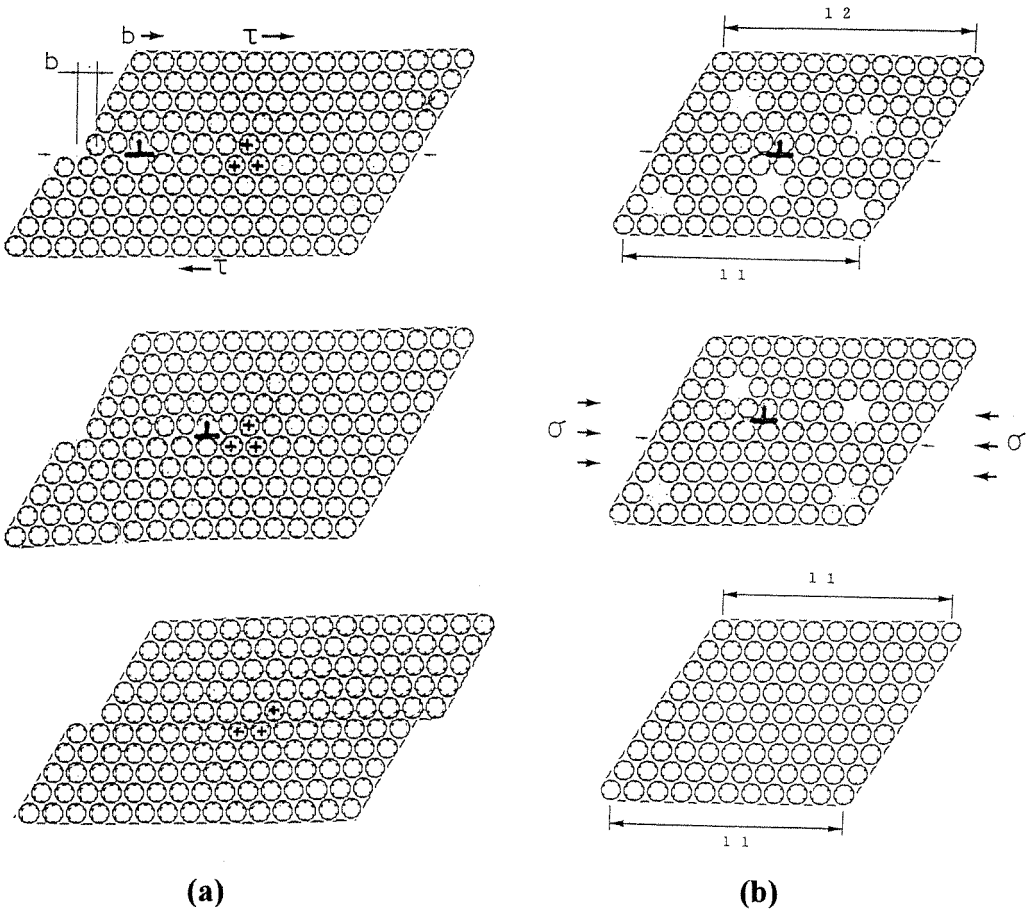

Figure 1: Two types of dislocation motion. (a) Glide motion. An edge dislocation (normal to the page) is passing through the crystal from left to right under a shear stress τ causing the top half of the crystal to displace by $\boldsymbol{b}$ compared to the bottom half. This slip vector $\boldsymbol{b}$ is called the Burgers vector, and the plane parallel to both $\boldsymbol{b}$ and the dislocation line is called the glide plane. We define the glide motion of a dislocation by its motion on the glide plane. The small displacements of individual atoms during the glide motion are cooperative motions of many atoms required by the glide motion. (b) Climb motion. Dislocation motion in the direction normal to the glide plane is called climb motion. In this figure, the edge dislocation is moving upward by absorbing vacancies under a compression stress σ. Then, the top half crystal is compressed by $\boldsymbol{b}$. For ice, interstitial water molecules are emitted instead of vacancies as described in section 2.6 (from Hondoh [5]).

energy stacking fault. Because, for ice I_h, a stacking fault lying on a basal plane has a very low energy, dislocations are stabilized by an extension on the basal planes [1, 40]. Glide motion of such a dislocation is restricted on the basal plane because changing the plane of motion (cross slip) requires a very large stress. Although short segments of a given dislocation move on prismatic planes faster than those on the basal planes, this type of the dislocation motion contributes little to the deformation of the whole specimen; although it is important for local deformations. Therefore, only the basal slip is observed on a macroscopic scale.

In this review article, I will explain the plasticity of ice from the above point of view. This viewpoint is supported by theory that is based on the fact that the stacking fault lying on the basal plane has a very low energy; however, the extended dislocations, or ribbon-like structure, have not yet been directly observed in ice.

2. Dislocations in ice

2.1 Dislocation criteria for slip systems in a crystal

According to dislocation theory [2], the possible slip systems in a given crystal can be predicted by the following criteria.

(1) Low self-energy requirement: Because the self-energy of a dislocation is proportional to the square of the Burgers vector length, only a few different types of dislocations with short Burgers vectors can exist in a real crystal.

$$E_d = \frac{Kb^2}{4\pi}\ln\left(\frac{\alpha R}{b}\right) \qquad (1),$$

where K is the energy factor expressed by the elastic constants, α the core parameter is approximately 2 for ice, and R the outer cutoff radius. When a dislocation lies along the center of a cylinder, R equals the cylinder's radius. For a regular dislocation array in a small angle grain boundary, R is half of the dislocation spacing. Thus, the self-energy E_d depends on the sample size and the dislocation arrangement. K equals μ for screw dislocations and $\mu/(1-\nu)$ for edge dislocations in isotropic continua, where μ and ν are the shear modulus and the Poisson ratio, respectively.

(2) Low Peierls-stress requirement: The Peierls stress τ_p is a maximum lattice resistance stress for glide motion of a dislocation, and according to Peierls-Nabbarro model it is given by:

$$\tau_p = \frac{2\mu}{1-\nu}\exp\left(-\frac{2\pi}{1-\nu}\cdot\frac{d}{b}\right) \qquad (2),$$

where d is a spacing of the glide planes and b the Burgers vector length. The magnitude of the Peierls stress drastically changes with the values of d/b, and hence depends on the crystal structure. Therefore, because low-index planes have a larger lattice spacing d, dislocation glides on low-index planes are predominant over those on higher index planes.

(3) Stacking fault restriction: When the energy of a stacking fault lying on a certain lattice plane is sufficiently low, the dislocation extends into a ribbon-like structure on the lattice plane. The motion of the extended dislocation is strongly restricted on the plane of the extension. Thermal activation to

constrict the extension is needed for a cross slip to other lattice planes.

2.2 Possible Burgers vectors and slip systems in ice

According to the above criteria, possible Burgers vectors of dislocations in ice are listed in Table 1. The vectors ***a*** and ***c*** are the translation vectors in the unit cell as shown in Fig. 2(a). Possible slip planes for the Burgers vectors are shown in Fig. 3. A brief explanation of a perfect dislocation and a partial dislocation is given in the caption of Fig. 2. The perfect dislocations are described first. Comparing the self-energies in Table 1, dislocation ***a*** is preferred over the others. The Peierls stress τ_p calculated by eq. (2) is a useful measure to predict the active slip systems in a given crystal. The *d*/*b* values in Table 1 suggest that the glide motion of dislocation ***a*** on the basal (0001), on the prismatic $\{10\bar{1}0\}$, and on the pyramidal $\{10\bar{1}1\}$ are equally likely candidates for the primary slip. Other slip systems by ***c*** and ***a***+***c*** are much less important because of larger *b* and smaller *b*/*d*.

However, since the stacking fault on the basal plane has a very low energy, as shown in Table 2 and explained in Fig. 2, a complete understanding of dislocation behavior in ice involves partial dislocations. A perfect dislocation ***b*** must dissociate into partial dislocations with smaller Burgers vectors $\boldsymbol{b}_1$ and $\boldsymbol{b}_2$ provided that $b^2 > b_1^2 + b_2^2$, and the energy of stacking-fault associated with this dissociation is sufficiently low. All of the perfect dislocations lying on the basal planes are stabilized by dissociating into two partial dislocations shown in Table 3 and in

Table 1: Dislocations and glide systems in ice.

Type of dislocation	Burgers vector		Self-energy*	*d* / *b***				
				(0001)	$\{10\bar{1}0\}$	$\{11\bar{2}0\}$	$\{10\bar{1}1\}$	$\{11\bar{2}2\}$
Perfect	***a***	4.52A	1	**0.61**	**0.58**		**0.61**	
	c	7.36A	2.7		0.35	0.31		
	a+***c***	8.63A	3.6		0.30		0.32 (0.22)	0.28 (0.17)
Partial	***p***	2.61A	0.33	**1.06, 0.35**		0.87		0.92 (0.55)
	c/2	3.68A	0.66		0.71	0.61		
	p+***c***/2	4.51A	1.0			0.50		

a = (1/3)<11$\bar{2}$0>, ***c*** = <0001>, ***a***+***c*** = (1/3)<11$\bar{2}$3>, ***p*** = (1/3)<10$\bar{1}$0>, and ***p***+***c***/2 = (1/6)<20$\bar{2}$3>. The bracket notation <hikl> expresses a group of equivalent directions whereas [hikl] is for a definite direction in a given coordinate. Plane index {hikl} for a group of equivalent planes, and (hikl) for a definite plane.

* For the self-energies, relative values are calculated by assuming constant *K* and *R* in eq.(1).

** For *d*/*b* values, the largest ones among different values for the same glide system are listed except for ***p*** (0001), for which the smaller *d*/*b* but an important candidate for an extended dislocation is also listed. The *d*/*b* value in bracket is calculated for a narrower gap of the same lattice planes. The cells with bold figures for *d*/*b* value indicate the glide systems that have been observed by experiments or strongly suggested by theoretical considerations based on experimental facts.

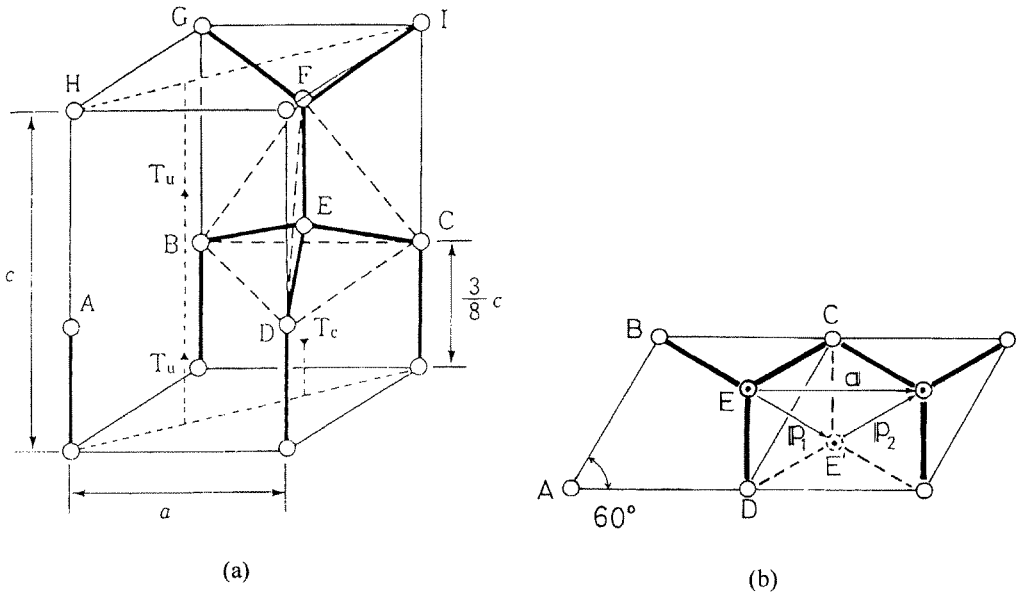

Figure 2: Crystal structure of ice I_h and stacking faults. (a) The unit cell of ice I_h. Water molecules sit on the open circles and are bonded with each other by hydrogen bonds marked by the thick lines. The lattice constants a and c are 4.52A and 7.36A, respectively. A tetrahedral bonding is shown by BCDF centered at E. T_u and T_c are the interstitial sites [6, 25]. (b) Stacking faults in ice. When the upper half crystal above E is translated by a vector $\boldsymbol{a}$, $(1/3)\langle 11\bar{2}0\rangle$, the crystal structure is identical with that before the translation, then the dislocation with this Burgers vector is called a perfect dislocation because it equals a perfect translation vector. In contrast, a different crystal structure is brought by the imperfect translation $\boldsymbol{p}_1$, $(1/3)\langle 10\bar{1}0\rangle$ because there is no water molecule at E' in the original crystal. However, tetrahedral hydrogen bonding can still form at E' as shown by the dotted lines. The dislocation with the Burgers vector $\boldsymbol{p}_1$ is called a partial dislocation. A partial dislocation always has a plane defect brought by the imperfect translation $\boldsymbol{p}_1$. Introduction of this type of plane defect changes the stacking sequence of the atomic layers from the original one; thus, it is called a stacking fault. For hexagonal crystals, this results in the stacking sequence of a cubic structure I_c.

Table 2: Stacking faults in ice [1, 3].

Plane	Fault vector	Fault energy*
	$\boldsymbol{p}$	~0.6 mJ/m^2
(0001)	$\boldsymbol{c}/2$	~0.9 mJ/m^2
	$\boldsymbol{p} + \boldsymbol{c}/2$	0.31 mJ/m^2
$\{10\bar{1}0\}$**	$\boldsymbol{p}$ (?)	

* The energy for the stacking fault $(\boldsymbol{p}+\boldsymbol{c}/2)$ on (0001) was measured by the XRT method [3], and other two above were multiplied by 2 and 3 according to the number of the cubic layers inserted by the stacking faults.

** Stacking faults on the planes other than (0001) have not been confirmed by observations nor theoretical considerations. However, behavior of the faulted loops on (0001) observed by XRT [4] implies the stacking fault on $\{10\bar{1}0\}$ during segregation process of self-interstitials.

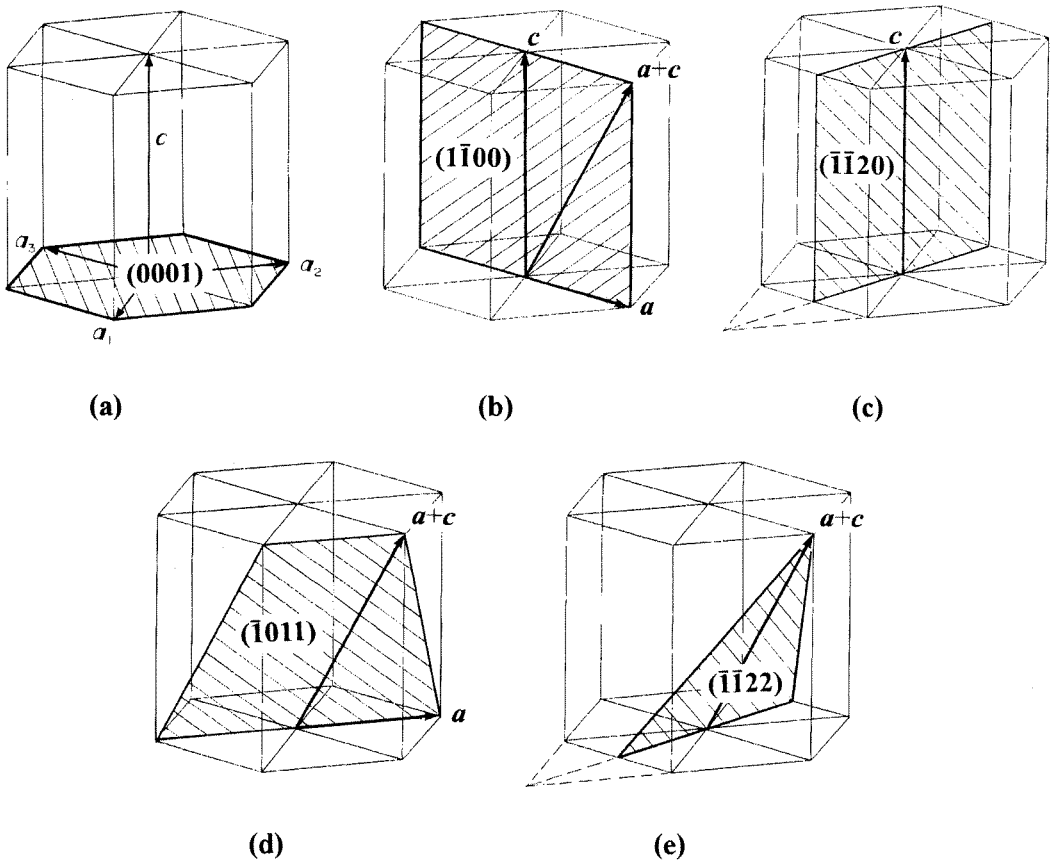

Figure 3: Burgers vectors and glide planes of dislocations in ice. (a) The plane expressed by the notation (0001) is called a basal plane. The primary slip occurs on this plane by the dislocations with the Burgers vector ***a***. (b) The prismatic slip on $\{10\bar{1}0\}$ can be caused by ***a***, ***c*** and ***a+c***. (c) The prismatic slip on $\{11\bar{2}0\}$ can be made only by ***c***. (d), (e) The pyramidal slip by ***a+c*** takes place on $\{10\bar{1}1\}$ or $\{11\bar{2}2\}$. For detail see Table 1.

Table 3: Extended dislocations in ice.

Plane	Perfect dislocation	Dissociation reaction	Extended width w
(0001)	***a***	$\boldsymbol{p}_1 + \boldsymbol{p}_2$	240 A (***a***: screw) 470 A (***a***: 60°) 550 A (***a***: edge)
(0001)	***c***	$\boldsymbol{c}/2 + \boldsymbol{c}/2$	1250 A
		$(\boldsymbol{c}/2 + \boldsymbol{p}_1) + (\boldsymbol{c}/2 - \boldsymbol{p}_1)$	2400 A (***p***: screw) 1800 A (***p***: edge)
(0001)	***a+c***	$(\boldsymbol{c}/2 + \boldsymbol{p}_1) + (\boldsymbol{c}/2 + \boldsymbol{p}_2)$	4100 A (***a***: screw) 4700 A (***a***: edge)

Figs. 4 and 5. The separation of the two partial dislocations in equilibrium is calculated by equating the repulsive force between the two partial dislocations with the attractive force due to the stacking fault. As shown in Table 3, the calculated equilibrium separations w are extremely large compared to those in other materials. This is because the widths for metals and semiconductors are about several times the Burgers vector. All types of dislocations in ice are widely extended on the basal planes. Both glide and climb motions of such widely extended dislocations are strongly restricted on the basal planes.

Because several molecular layers of the cubic structure I_c occur by introducing a stacking fault as shown in Fig. 4, we can calculate the energy difference between hexagonal ice I_h and cubic ice I_c from the measured stacking fault energy. It is 16 J/mol, or 0.00017 eV per molecule. Therefore, unusual nature of dislocations in ice originates in their very small energy difference between I_h and I_c, although I_h is more stable than I_c at all temperatures down to 0 K.

2.3 Nonbasal glide motion of dislocations

In addition to the primary slip system $<11\bar{2}0>/(0001)$, secondary slip systems by nonbasal glide motions of dislocations are needed for continuous deformation of polycrystalline ice. As a result of the dissociation of basal dislocations, nonbasal dislocations arise as short segments as illustrated in Fig. 6(a). The nonbasal segment is a jog or super jog of the basal dislocations according to the current terminology, but the height of the jog in ice is extremely large - about 0.01mm. This was suggested by observations of a temperature change that generated the prismatic edge-

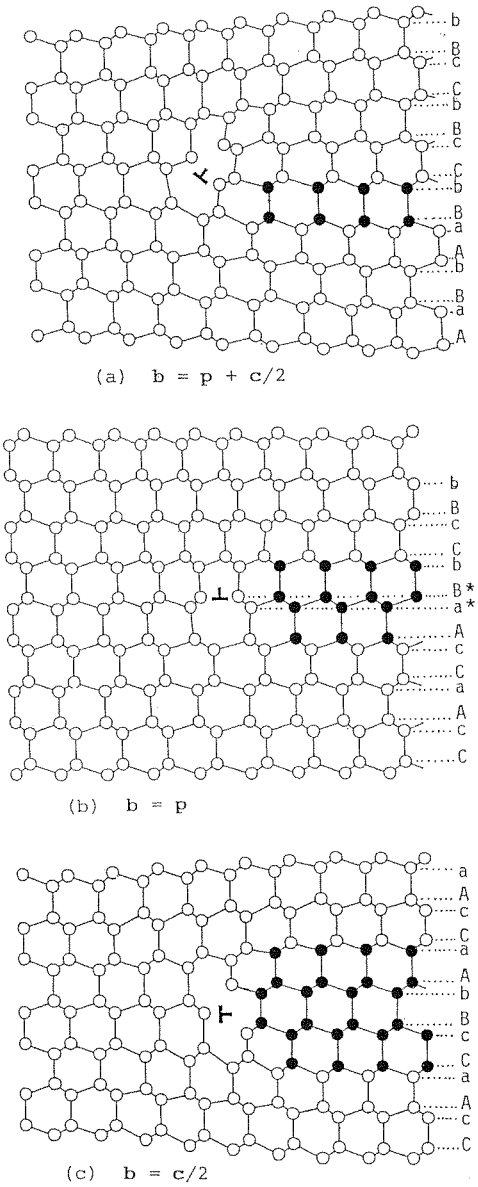

Figure 4: Partial dislocations in ice. These figures illustrate atomic arrangements around three possible partial dislocations, (a) $\boldsymbol{b}=\boldsymbol{p}+\boldsymbol{c}/2$, (b) $\boldsymbol{b}=\boldsymbol{p}$, and (c) $\boldsymbol{b}=\boldsymbol{c}/2$. The stacking sequences of the atomic layers indicated by the filled circles are different from the original ones (open circles). The stacking fault has no difference in the nearest neighbors with ice I_h as shown in Fig. 2, but it has second nearest neighbors the same those in the cubic structure I_c. (from Fukuda et al. [1])

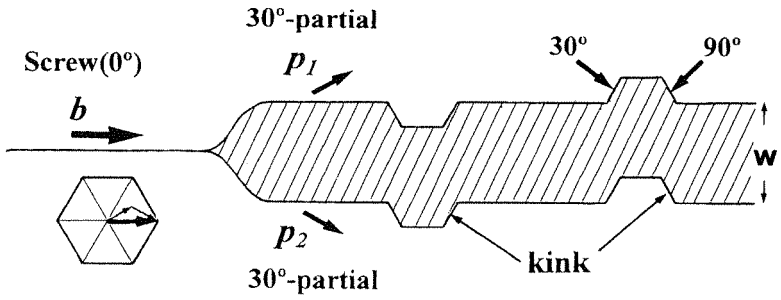

(a)

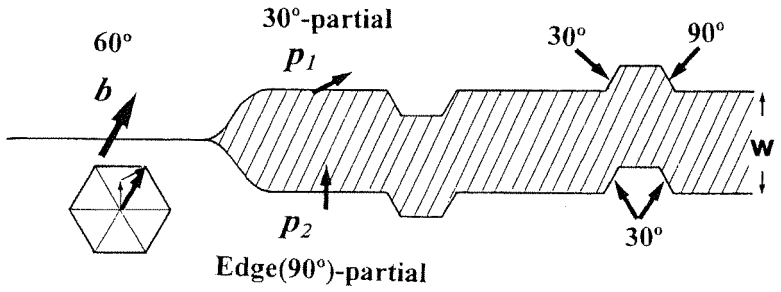

(b)

Figure 5: Extended dislocations in ice. The perfect dislocation with the Burgers vector $\boldsymbol{a}$ dissociates into two partial dislocations with the Burgers vectors $\boldsymbol{p}_1$ and $\boldsymbol{p}_2$, where $\boldsymbol{a} = \boldsymbol{p}_1 + \boldsymbol{p}_2$, to reduce the total self-energy of the dislocation. (a) screw dislocation and (b) 60°-dislocation lying along the Peierls trough are illustrated. The screw dislocation dissociates into two 30°-partial dislocations, whereas the 60°-dislocation dissociates into edge (90°)- and 30°-partial dislocations. In ice, the width w is very large as shown in Table 3, and therefore the double kink formation on the two partials must not correlate each other.

dislocation dipoles from basal dislocations [6]. We do not know if the nonbasal short segments are dissociated; however, an extended width must be very small even if dissociated because a low energy stacking-fault should not occur on nonbasal planes. Therefore, all nonbasal dislocations will be assumed to be nondissociated. A dislocation with arbitrary shape turns gradually to be parallel to the basal plane because the segments lying on the basal plane have a strong tendency to elongate. Therefore, a general dislocation should evolve into the stable terraced structure sketched in Fig. 6(a).

For a cross slip of the basal glide dislocations (Burgers vector $\boldsymbol{a}$) to other non-basal planes, the extended dislocations must constrict. However, this is not possible for such widely extended dislocations except at surfaces. The cross slip of a basal dislocation to a prismatic plane was

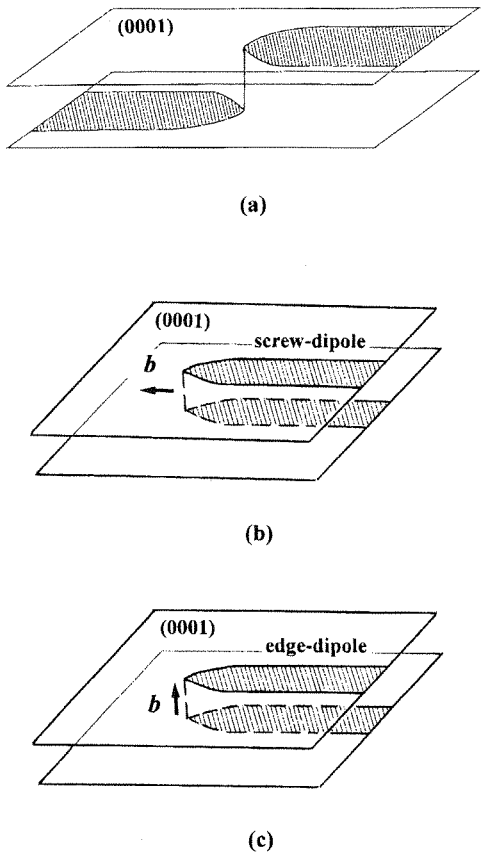

Figure 6: Possible configurations of nonbasal dislocations in ice. (a) A terraced structure of a dislocation in ice [11]. The step height observed by XRT is of the order of 0.1 mm [7, 20, 41]. Basal segments with the Burgers vector ***a*** are glissile, but others with ***c*** or ***a+c*** are sessile. Nonbasal segments are glissile on the planes given in Fig. 3. (b) Formation of a screw dislocation dipole with the Burgers vector ***a*** led by an edge segment gliding on the nonbasal plane [7, 20]. Basal segments are glissile. (c) Formation of an edge dislocation dipole with the Burgers vector ***c*** or ***a+c*** led by a screw segment gliding on the nonbasal plane. Basal segments are sessile. See also Fig. 7.

observed by x-ray topography, which was explained by constriction of the extended dislocation at the surface [1]. For stresses in ice sheets, nonbasal glides are mainly caused by the short segments of dislocations.

Edge dislocations with the Burgers vector ***a*** can glide on the prismatic $\{10\bar{1}0\}$ or the pyramidal $\{10\bar{1}1\}$ as shown in Fig. 6(b). The edge segment is followed by a dipole of screw dislocations that are glissile on the basal planes. Then, a source of dislocations can effectively operate to generate the same type of dislocations. Successive motion of such edge segments produces a step on the surface as shown in Fig. 7(b). This deformation mechanism was first proposed by Fukuda [7], and the surface steps were observed by Muguruma [8] (reproduced in [9]). Because the nonbasal dislocation is bound by the extended basal dislocations, this slip deformation cannot sweep through the entire crystal; successive motion of the dislocations is blocked by previous dislocations. A group of dislocations was observed by x-ray topography in this deformation mode [9, 10]. Comparing this deformation mode with that by the basal slip shown in Fig. 7(a) indicates that deformation of the entire crystal by this mechanism is much more difficult than the basal slip despite the higher mobility of the nonbasal segments than that of the basal dislocations (see Table 4).

Dislocations with the nonbasal Burgers vectors ***c*** or ***a+c*** are frequently observed by x-ray topography [10], but all of them lie on the basal planes, another result of the low stacking fault energy as described above. Short segments of screw dislocations connect the dislocations extended on the basal planes as shown in Fig. 6(c). The resulting deformation is shown in Fig. 7(c). The screw segments moving on the pyramidal planes deform the specimen, but this deformation is limited to a narrow slip

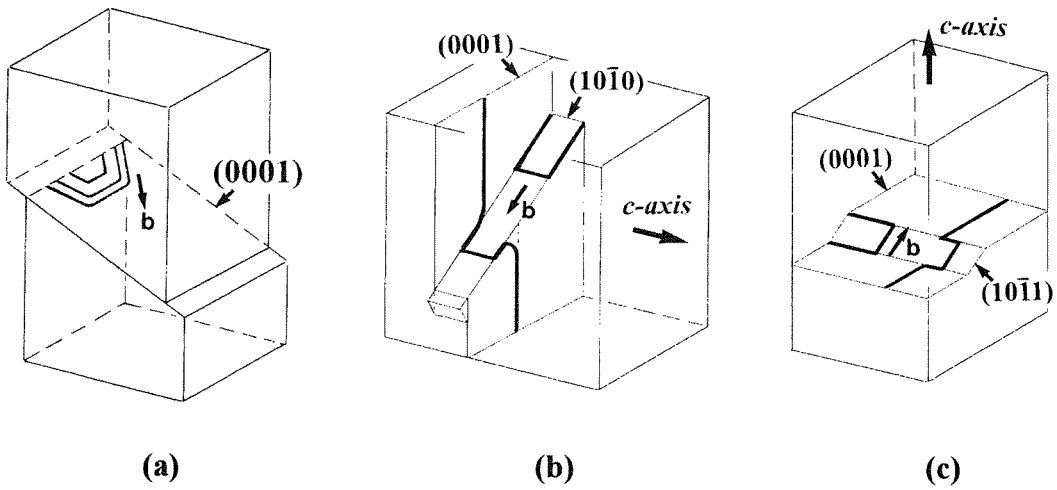

Figure 7: Deformation resulting from dislocation glide in ice. A tensile force is applied in the vertical direction. (a) Deformation by basal dislocations ***a***. Continuous, long slip lines appear on the surface. (b) Deformation by prismatic dislocations ***a***. Glide motion on the pyramidal planes $\{10\bar{1}1\}$ is also possible (see Fig. 3) [9, 12, 41]. Characteristic surface-steps form. Note that successive dislocation generation at the same source is allowed because the basal segments are glissile. (c) Deformation by pyramidal dislocations ***a+c***. A trace of shear appears on the surface, but surface-steps are not expected, and successive generation of the dislocations from the same source are not expected because of the sessile basal segments. Glide motions on the pyramidal planes $\{11\bar{2}2\}$ and on the prism planes $\{10\bar{1}0\}$ are also possible (see Fig. 3). Similar way of deformation is expected for dislocations ***c***.

plane elongated normal to the loading axis. For the screw dislocations, no surface steps appear, but the trace of shear can appear on the surface. Although this type of dislocation behavior had not been observed until now, the prismatic slip of this type can be seen in the paper by Wei and Dempsey [13]. Through etching, they observed a surface trace parallel to $\{10\bar{1}1\}$ in the specimen deformed parallel to the c-axis. They explained the trace as a result of pyramidal slip, although the mechanism in their explanation is different from that given here.

Dislocation mobility of this type must be much smaller than that of the prismatic plane because of the higher Peierls stress and the zigzag slip planes. In addition, the nonbasal screw segment is followed by a dipole of sessile edge dislocations lying on the basal planes. Therefore, successive generation of this type of dislocation is significantly reduced. Therefore, this type of deformation is more difficult than that by nonbasal glides of dislocations ***a***.

In early studies on the deformation bands in ice, most of the nonbasal glide systems described above were proposed to explain the etch channels observed on the basal planes [14, 15]. Those results are probably explained by the nonbasal segments intersecting the free surface.

Other phenomena related to nonbasal deformation is void formation observed during tensile deformation normal to c-axis [16, 17]. This phenomenon was explained by segregation of vacancies generated by climb motion of the nonbasal edge dislocations [17]. The edge segment shown in Fig. 6(b) can move perpendicular to its

glide plane (climb motion) when a normal stress parallel to the Burgers vector is applied. In tensile deformation, the climb occurs downwards in Fig 1(b), and then vacancies are generated. Supersaturated vacancies can nucleate as voids. These voids should have a plate-like shape parallel to a basal plane because of low surface energy of the basal plane. If the supersaturation is low, a thin plate-like void turns into a dislocation loop too small to be seen by microscope, but at sufficiently high supersaturation, the voids grow into large thick plate-like cavities visible by microscope. However, as described in section 2.6, only a small amount of climb motion is expected as compared to that of glide motion under a same stress level. Because successive glide motion of the nonbasal segments is restricted in the slip bands as described above, many dislocations climb and generate a significant number of vacancies. Consequently, cavities formed in rows parallel to $<11\bar{2}0>$ have been observed [16, 17]. In compressive deformation, self-interstitials are generated instead of vacancies and must form dislocation loops, although this has not been observed yet.

In deep ice sheets, however, voids are not stable under high hydrostatic pressure so that supersaturated vacancies should instead form dislocation loops. However, the above mechanism for void formation can occur in ice cores after drilling; the anisotropic expansion of ice crystals after pressure release causes stress that drives the climb motion of the edge segments, which then can form voids. Formation of cavities in deep ice cores can be explained by this mechanism followed by segregation of gas molecules dissolved in ice.

2.4 Critical stresses for glide motions of dislocations

A dislocation moves on its glide plane when a resolved shear stress on the plane exceeds the Peierls stress τ_p. However, for ice $\tau_p \approx 0.01\mu$ (i.e., 35MPa) even for the largest d/b. Ice subjected to this high stress must be fractured without plastic deformation. To surmount the Peierls barrier at lower stresses, thermal activation is required. Therefore, ice can be deformed only at elevated temperatures. In contrast, for soft metals such as copper and aluminum, $\tau_p \approx 10^{-6}\mu$ because of a large d/b, and therefore thermal activation is not required for glide motion of dislocations in those materials; they are ductile even at low temperatures. Thermally activated motion of dislocations does not require stress to surmount the lattice resistance. However, dislocations are frequently pinned by some obstacles that require stress to move past.

The critical stress to move in a certain slip system can be defined as the stress to push the dislocation through two pinning points. That is $\tau_c \approx \mu b/L$ for the pinning distance L. In pure ice without any impurity obstacles, the basal glide dislocations are pinned or dragged by the nonbasal segments, and the motion of the nonbasal glide dislocations are limited by the basal dislocations as described in the preceding section. Thus, the difference in the critical stress between the basal and the nonbasal glides by the dislocation $\boldsymbol{a}$ is caused by the difference in the length of the dislocation segments that can move freely. Although the pinning distance depends on specimens and varies also with deformation, for a rough estimate of τ_c we assume that $L \approx$ 1mm for the basal and 0.01mm for nonbasal as a typical pinning distance. Then, τ_c is about 10^{-3} MPa for the basal glide, and 0.1 MPa

for the nonbasal glide by ***a***. These stresses have produced dislocation motion as observed by x-ray topography [9, 19-21, 36, 37].

For nonbasal glide by ***a***+***c***, the self-energy of the dislocation is 3.6 times larger than that for ***a***, and the Peierls stress τ_p calculated by eq.(2) is one order of magnitude larger than that for ***a***. Compared to that with glide ***a***, generation of this type of dislocation is less likely and its glide much more difficult. However, if the lengths of the nonbasal segments are the same, then the critical stress τ_c calculated by the above equation is about that with the nonbasal glide by ***a***. Therefore, the pyramidal slip by ***a***+***c*** should be possible as described in the preceding section. Similar arguments should also apply to the nonbasal glide by ***c***.

All of the above estimates for the nonbasal glides seem impractical because stresses several orders of magnitudes larger are required when ice is deformed without shear stress on the basal plane [16, 18]. This apparent discrepancy is due to the deformation modes shown in Fig. 7. The nonbasal glides cause localized deformation only: unlike deformation by basal glide, they contribute little to the deformation of the entire crystal. Therefore, at a given deformation rate, much larger stresses are needed. However, nonbasal glide must be important for relaxing local stress concentrations caused by deformation; for instance, more than five independent slip systems must act in a region narrow compared to the height of the dipole in Fig. 6.

2.5 Mobility of dislocations for glide motion

The measured velocities of dislocations V_d, both on basal and nonbasal glide motions, are proportional to an applied resolved shear stress τ [9, 20, 21]. Therefore, the mobility M can be defined by

$$V_d = M\tau \tag{3}.$$

M can be expressed by

$$M = M_0 \exp\left(-\frac{Q}{kT}\right) \tag{4}.$$

Values of M_0 and the activation energy Q determined for the dislocations ***a*** are summarized in Table 4. The values of M at –20 °C are also included in the table. The mobility for the nonbasal edge dislocation is more than five times larger than those of the basal dislocations. For the basal dislocations, M for screw dislocations is smaller than the 60°-dislocations.

Dislocation motion in a crystal with a high Peierls stress such as ice is described by the kink diffusion model [2]. The dislocation velocity V_d is then

$$V_d = hC_K V_K \tag{5},$$

$$C_K = \frac{2}{a}\frac{1}{\exp(F_K/kT)+1} \tag{6},$$

$$\approx \frac{2}{a}\exp(-F_K/kT) \tag{6'},$$

$$V_K = \frac{bd\tau}{kT}a^2\nu\exp\left(-\frac{W_m}{kT}\right) \tag{7},$$

where C_K and V_K are the concentration and velocity of kinks, respectively, h the periodicity of the Peierls potential, F_K the kink formation free energy, and W_m the activation free energy for the kink migration. Although the approximate equation (6') includes a rather large error in the present case [21], we use this equation for easier

Table 4: Mobility of dislocations with the Burgers vector of 1/3 <11 $\bar{2}$ 0>.

	Q (eV)	M_0 (m s^{-1} Pa^{-1})	Mobility (μm s^{-1} MPa^{-1}) at -20°C	
Basal screw	0.756	1500	1.3	Okada et al. [21]
	0.95		1.0	Shearwood et al. [20]
Basal 60°	0.69	130	2.6	Okada et al. [21]
	0.87		2.0	Shearwood et al. [20]
Basal curved	0.62	6.4	2.9	Yamamoto*
			2.6	Yamakami et al. [19]
Non-basal edge	0.61	24	14.5	Hondoh et al. [9]
	0.63		22.0	Shearwood et al. [20]

*quoted by Fukuda et al. [1]. Note that M_0 depends on T in the kink diffusion model.

description of the energy relations: i.e., $Q \approx F_K + W_m$, $F_K = E_f + S_f$, and $W_m = E_m + S_m$, where E and S denote the energy and entropy, respectively related to the formation (subscript f) and migration (subscript m) of kinks.

One difficulty is that experimental gives V_d but not C_K nor V_K. Hondoh [22] proposed a new method to determine C_K and V_K separately by observing a transient behavior of dislocations from a curved shape to a straight line parallel to the Peierls trough. He estimates F_K in eq.(6') as approximately 0.15 eV on the basis of observations by x-ray topography. When a dislocation lies off the Peierls trough, it contains geometrical kinks as well as thermal kinks [22]; these skew segments of the dislocation move faster than the segments lying in the trough. Okada et al. [21] developed this idea further; their method uses the observed curvature of dislocations where they intersect the troughs to calculate a kink density. Using this, the kink formation energy E_f and formation entropy S_f in Table 5 were obtained. Table 6 has the kink velocity V_K, from eq.(5); and also the kink migration energy E_m, and the kink migration entropy S_m, from the above energy relations.

Considering the results by Okada et al. in Tables 4–6, we have a comprehensive picture for understanding the mobilities of dislocations in ice. For the motion of curved dislocations, no thermal kink formation is needed because a sufficient number of geometrical kinks already exist. For 'basal curved' and 'non-basal edge' in Table 4, the activation energy for dislocation motion is only the kink migration energy 0.62 eV.

For glide motion of basal dislocations, the difference in the activation energies between the screw and 60°-dislocations is due to the difference in their kink formation energies. Because the basal dislocation dissociates into partial dislocations, this difference is because the screw dissociates into two 30°-partials, whereas the 60°-dislocation dissociates into an edge and 30°-partials as shown in Fig. 5. The edge partial has a kink with the angle of 30°, but the 30°-partial has the angle of 90° or 30°. For

Table 5: Kink formation parameters in ice [21].

Dislocation type	E_f (eV)	S_f / k
a screw	0.16	4.9
a 60°	0.08-0.09	2.2-2.5

Table 6: Kink migration parameters in ice [21].

Dislocation type	E_m (eV)	S_m / k
a screw, 60°	0.62	11.3-11.6

a rough estimation, assume the kink energy by $\mu b_p^2 h$ (for screw component) and $\mu b_p^2 h/(1-\nu)$ is the edge component. This gives 0.17 eV for the 30°-kink and 0.23 eV for the 90°-kink: the formation energy of a kink on the edge partial is smaller than that on a 30°-partial; therefore, there should be a higher concentration of thermal kinks on the edge partial than on the 30°-partial. Thus, the 60°-dislocation should have a larger mobility than a screw dislocation.

The large difference in the activation energies from Okada et al. [21] and Shearwood and Whitworth [20] is not understood. Because their mobility data above –20 °C are approximately the same, the large difference comes from the very low mobilities at lower temperatures by Shearwood and Whitworth. If we instead use their activation energy, the kink formation energy is about 0.3 eV. As pointed out by Hondoh [22], this large kink formation energy is not consistent with the dislocation behavior observed by x-ray topography. In addition, most of the deformation experiments on single crystals of ice indicate an activation energy of 0.62-0.81 eV, which is in good agreement with the result of Okada et al. [21].

Problems related to the mechanism of kink migration and the high concentration of kinks discussed in [21] remain unsolved, but a meaningful discussion on these topics would be too long for this brief review. Impurity effects on the dislocation velocity are also important topics because impurity doping softened ice according to early deformation experiments [23, 38]. However, a significant effect on dislocation velocities had not been observed until Hu et al. reported larger velocities in HCl doped ice [37]. This topic too will be skipped.

Higher mobilities close to the melting temperature were reported by Yamakami et al. [19] and by Perez et al. [36] with their core melting theory. This phenomenon must be due to unknown properties of dislocations as described by Okada et al. [21]. At higher temperatures and at lower stresses, skewed dislocations move without changing; they do not tend to become parallel to the Peierls trough because of higher density of thermal kinks. There are no anomalies in dislocation velocities close to the melting temperature. Consequently, softening of polycrystalline ice close to the melting temperature observed in deformation experiments must be due to grain boundary processes as discussed in section 4.3.

2.6 Climb motion of dislocations

Motion of dislocations perpendicular to a glide plane is called climb motion as shown in Fig. 1(b). As described in section 2.3, this type of dislocation motion emits and absorbs point defects. This type of dislocation motion also deforms a crystal, although it is relatively slow deformation compared to the glide motion. For an isolated dislocation with an edge component of the Burgers vector $\boldsymbol{b}_e$, the velocity of climb driven by the normal stress σ is given by

$$V_c \cong \frac{D_{SD}\Omega\sigma}{b_e kT} \quad (8),$$

where D_{SD} is a self-diffusion coefficient and Ω is the molecular volume [2]. Comparing this equation with eq.(3), the factor $D_{SD}\Omega/b_e kT$ is the mobility for climb motion. For the dislocation *c*, the mobility at the melting temperature is about 0.06 μm $(MPa)^{-1}s^{-1}$, which is more than two orders of magnitudes smaller than that for glide motion. In addition, unlike the glide motion, climb motion is significantly hindered by climb motion of other dislocations because this motion is associated with diffusion over long distances. Therefore, the above value must be an upper limit of the mobility.

When the concentration of self-interstitials C differs from that in equilibrium C_0, a climb force (osmotic force) on an edge dislocation is

$$F_{os} = \frac{kTb}{\Omega} \ln\left(\frac{C}{C_0}\right) \quad (9).$$

This osmotic force is comparable to a climb force by a normal stress $\sigma = (kT/\Omega)\ln(C/C_0)$. When ice is cooled from −10 °C to −20 °C, the supersaturation C/C_0 becomes 2, its maximum value (see section 3.1). Then, the normal stress of 74 MPa to drive the climb motion is comparable to this osmotic force. Thus, a temperature change is a much more effective driving force for climb than stress.

The climb motion of the dislocation ***a+c*** is also frequently observed after a temperature change. This is always restricted on the basal planes, but never on the planes normal to the glide planes of this type of dislocation. This is mainly because of the wide extension of the dislocation as discussed in section 2.2. Because of this large stress by the osmotic force, constricting the extended dislocation is difficult.

3. Nature of point defects in ice

For point defects in ice, we should distinguish those violating the ice rules (point defects from hydrogen atoms) from those violating the lattice periodicity (point defects of the whole water molecule). The former, ionic and Bjerrum defects, largely determine the electrical properties of ice. Their nature and properties are described in detail in the literature [23].

3.1 Self-interstitials in ice

The point defects of a whole molecule, vacancies and self-interstitials, will diffuse in a crystal. If we add the contributions from vacancies and self-interstitials to the self-diffusion coefficient D_{SD}, then

$$D_{SD} = C_V D_V + C_{SI} D_{SI} \quad (10),$$

where C_i and D_i denote the equilibrium concentration in mole fraction and the diffusion coefficient of the point defects, respectively for i = V(vacancy) or SI(self-interstitial). In ice, self-interstitials out-number vacancies, at least above −50 °C, or $C_{SI} > C_V$ [24], and the tracer-diffusion coefficient is approximately equal to the product of C_{SI} and D_{SI} measured separately, or $D_{SD} \approx C_{SI} D_{SI}$. Thus, the interstitial mechanism dominates self-diffusion in ice [6, 24, 25]. The concentrations and diffusivities of the point defects in ice are tabulated in Table 7.

All of the self-interstitial parameters included in the following equations are given in Table 8.

Table 7: Point defects and diffusion coefficients in ice.

	Concentration at 0 °C	Formation energy	Diffusion coefficient at 0 °C	Activation energy
Self-interstitials	2.8×10^{-6} mole fract.	0.40 eV	2.0×10^{-9} m^2/s	0.16 eV
Vacancy [47]	$\gtrsim10^{-8}$	~0.35		~0.34
Self-diffusion coefficient (ice) [6]			5.6×10^{-15}	0.56
Self-diffusion coefficient (icc) [46]			4.1×10^{-15}	0.62
Self-diffusion coefficient (QLL on surface) [43]			3.2×10^{-13}	0.24
Self-diffusion coefficient (water)			1.3×10^{-9}	0.19

$$C_{SI} = \frac{1}{2}\exp\left(\frac{S_f}{k}\right)\exp\left(-\frac{E_f + pV_f}{kT}\right) \quad (11),$$

$$D_{SI} = D_0 \exp\left(-\frac{E_m + pV_m}{kT}\right) \quad (12).$$

Although the detailed properties of point defects are not described in this review article, some description is necessary. One water molecule sits at an interstitial site per 10^6 water molecules sitting on the regular sites of ice lattice. The interstitial water molecule moves to an adjacent site by jumping through the lattice. This jumping frequency is about 10^{10}s^{-1}. When tracer molecules such as $H_2{}^{18}O$ and $D_2{}^{16}O$ replace the ordinary water molecules, the same fraction (10^{-6}) of the tracer molecules are interstitials. However, their jump frequencies must be smaller than that of the ordinary water molecule because of their larger mass. Therefore, the tracer diffusion coefficient must be slightly smaller than D_{SD} stated above.

The primary source or sink for self-interstitials is the free surface. To generate a self-interstitial, a water molecule is removed from the surface, then put in an interstitial site. The work done by this process equals $E_f + pV_f - TS_f$. The formation volume V_f is the volume change of the crystal by introducing a self-interstitial. Because V_f is negative, C_{SI} increases with pressure. Grain boundaries are also effective sources and sinks for self-interstitials. Inside the crystal, edge dislocations are effective sources and sinks. Although it requires more energy, pair formation of a self-interstitial and a vacancy can occur away from any defect. This pair formation mechanism must occur to supply water molecules to climbing edge dislocations of the nonbasal slips discussed in section 2.3.

In polycrystalline ice, there exist fast diffusion paths such as grain boundaries and dislocation walls. Although there are no reliable data of diffusion coefficients of water molecules through grain boundaries D_{GB}, we can estimate its magnitude using data in Table 7. Comparing the self-diffusion coefficient of water with that of ice, we can understand that the large

Table 8: Self-interstitial parameters in ice [6, 22, 24, 25, 42, 44].

E_f	S_f	V_f	E_m	D_0	V_m
0.40 eV	4.9k	-0.26Ω*	0.16 eV	1.8×10^{-6} m^2/s	0.40Ω

* V_f = -0.8Ω was given in [42], but more reliable data by [44] is adopted.

difference between the two is due to C_{SI}. That is, the mobility of self-interstitials in ice does not differ from that in water. The difference is due to the large difference in the number of mobile molecules between water and ice. Therefore, the diffusion coefficient through a fast path must be between the two with a value depending on the fractional concentration of mobile molecules. For quasi-liquid layers (QLL) on the free surfaces, for example, the diffusion coefficient measured is by two orders of magnitude larger than that in ice as shown in Table 7. A plausible value of D_{GB} probably is of the same order of magnitude.

In deep ice cores, dislocation walls or sub-boundaries must be important for the fast diffusion path. The grain size measured by the conventional optical method is about 1 mm in deep ice sheets. This is sufficiently large to ignore the fast diffusion through GB when a total amount of mass transport is discussed because the thickness of GB is much smaller than 1 μm. However, it was observed by x-ray topography that such a large grain is composed of many subgrains with very small misorientations [39]. We also do not know the diffusion coefficient through these sub-boundaries; however, we should consider the microstructure into consideration in case of deep ice sheets.

3.2 Diffusion of gas molecules in ice

Diffusion of atmospheric gases in ice sheets below the close-off depth has been ignored until recently. Because molecular fractionation was found with respect to transition of air bubbles to air hydrates [26], molecular diffusion in ice sheets is one of the most important processes in ice core physics. This topic is discussed in detail by Ikeda et al. [27] in this volume. They assume an interstitial mechanism for diffusion of N_2 and O_2 to estimate their diffusion coefficients, which have been not measured until now. However, for larger gas-molecules, the vacancy mechanism could also influence diffusion.

4. Plastic deformation of ice

4.1 Deformation by diffusion of point defects

Crystalline materials are also deformed by the diffusive flow of point defects such as vacancies and self-interstitials. When a block of crystal is subjected to uniaxial compression, vacancies are driven from the tensile side to the compression side, and vice versa for self-interstitials. This driving force is due to interaction between the applied stress and the local stress associated with the point defect. The self-interstitial, for example, exerts compression stress owing to local volume expansion; therefore, it has an attractive interaction with the tensile stress and a repulsive interaction with the compression stress. The steady-state strain rate by this type of deformation is

$$\dot{\varepsilon}_{SD} = \frac{B\Omega}{kTd^2}\left(D_{SD} + \frac{\pi\delta}{d}D_{GB}\right)\sigma \qquad (13),$$

where d is the grain diameter, δ the thickness of the boundary, Ω is the molecular volume, and σ is the applied stress. The parameter B was calculated by many different models, B=20 for example [28]. The first term in the right hand of eq.(13) is Nabbarro-Herring (NH) creep, the second is Coble creep.

If we assume that D_{GB}/D_{SD} is about 10^3 as discussed in the preceding section, the NH creep is dominant over the Coble creep for grain sizes larger than $10^3\delta$. Because the

GB thickness δ must be about 10^{-9} m, the NH mechanism is dominant over the Coble mechanism in deep ice sheet because of the very large grain size. However, if the sub-boundary structure significantly affects the diffusion as described in the preceding section, faster deformation by this mechanism is possible.

Azuma calculated the ratio of diffusion creep to the dislocation creep according to the deformation mechanism map, and showed that the ratio becomes significant in deep ice sheets [45].

4.2 Deformation of ice by dislocations

As a macroscopic output of either glide and climb motions of dislocations, ice is deformed at a strain rate

$$\dot{\varepsilon} = \rho_m b \overline{V} \qquad (14),$$

where strain ε is brought by the Burgers vector component $\boldsymbol{b}$, and ρ_m is a density of mobile dislocations, and $\overline{V}$ the average velocity of the dislocations. Deformation systems in ice, or a strain component ε_{ij} given by glide or climb motion of dislocations with a different Burgers vector $\boldsymbol{b}$, are summarized in Table 9. For both glide and climb, the dislocation velocity is proportional to the stress exerted on the dislocation σ (or τ) as described in the preceding sections. It is much more complicated to derive the mobile dislocation density ρ_m as a function of σ. At a steady state of dislocation interactions when the generation rate of dislocations equals the annihilation rate, ρ_m can be expressed as proportional to σ^2. Therefore, the power law 3, $\dot{\varepsilon} \propto \sigma^3$, holds for plastic deformation of polycrystalline materials (for example, see [29]).

For deformation of polycrystalline ice, we can assume that only the basal slip contributes to the macroscopic strain. Then, ρ_m and b in eq.(14) should be those for the basal dislocations $\boldsymbol{a}$. However, the average velocity should be modified to include dislocation interactions. Because glide motions of the dislocations are hindered by strong interactions between them and generated by the deformation itself as briefly discussed in the next section, the deformation rate must be limited by annihilation rate of the dislocations. When the dislocations are annihilated by their climb motion of an average distance L_c, and this allows the basal glide in an average distance L_g, the glide velocity equals L_g divided by the average life time L_c/V_c. Therefore, $\overline{V}$ in eq. (14) should be replaced by $(L_g/L_c)\ V_c$. The climb velocity V_c can be expressed in terms of the jog density C_j, the jog velocity V_j and the jog height h as,

$$V_C = hC_jV_j \qquad (15),$$

$$= \frac{bh}{kT} D_{SD} C_j \sigma \qquad (16).$$

Equation (16) is valid only for the low jog-density case because jog formation on basal dislocations extended on the basal planes is very difficult to treat as discussed in section 2.3. Then, we obtain the strain rate as

$$\dot{\varepsilon} = \kappa D_{SD} C_j \sigma^3 \qquad (17),$$

where κ is a parameter that depends on details of the mechanism (see for example [29]).

Equation (17) suggests that the activation energy for plastic deformation of polycrystalline ice Q_p equals the sum of the

Table 9: Deformation systems in ice.

Type of motion	Burgers vect. $\boldsymbol{b}$	Plane of motion	Strain component	Comments
Glide	(1/3)<11 $\bar{2}$0>	(0001)	ε_{13}, ε_{23}	Primary, any segment*1
		{10 $\bar{1}$0}	ε_{12}, ε_{11}, ε_{22}	2nd, Edge segment*2
		{10 $\bar{1}$1}	ε_{12}, ε_{11}, ε_{22}	2nd, Edge segment*2
	<0001>	{10 $\bar{1}$0}	ε_{13}, ε_{23}	Screw segment*3
		{11 $\bar{2}$0}	ε_{13}, ε_{23}	Screw segment*3
	(1/3)<11 $\bar{2}$3>	{10 $\bar{1}$0}	except ε_{33}	Screw segment*3
		{10 $\bar{1}$1}	all	Screw segment*3
		{11 $\bar{2}$2}	all	Screw segment*3
Climb	<0001>	(0001)	ε_{33}	
	(1/3)<11 $\bar{2}$3>	(0001)	ε_{33}	
	(1/3)<11 $\bar{2}$0>	normal to {10 $\bar{1}$0}	ε_{11}, ε_{22}	Void formation*4

*1, *2, *3; see Fig. 7. *4; see section 2.3.

activation energy for self-diffusion Q_{SD} and the jog formation energy on the basal dislocations Q_j. Therefore, Q_p should be larger than Q_{SD}. The experimental data on Q_p are 0.6-0.8 eV below −10 °C and 1.0-1.4 eV above −10 °C. Q_{SD} is 0.56-0.62 eV as shown in Table 7, and then Q_j should be smaller than 0.2 eV below −10 °C.

For the deformation mechanism above −10 °C, we can assume that the dislocations are mostly annihilated in the grain boundaries (GB). In this case, jog formation can be ignored but the GB thickness δ should be included. Then, $D_{SD}C_j$ in eq.(17) should be replaced by $D_{GB}\delta$. We know nothing quantitative about δ, but it must strongly depend on temperature to give a larger activation energy in eq.(17).

4.3 Grain-boundary effects on the plastic deformation of ice

Grain boundaries (GB) play an important role in the plastic deformation of polycrystalline materials. GBs are the most effective sources and sinks for dislocations [30] as well as for point defects. GB sliding causes stress concentrations at GB intersections, which generate dislocations. However, their most important role is as a barrier for dislocation motion.

When a dislocation with Burgers vector $\boldsymbol{b}_1$ moves by its glide motion from one grain to become $\boldsymbol{b}_2$ on another grain, a GB dislocation $\boldsymbol{b}_{GB}$ is left on the GB to conserve the total Burgers vector, or $\boldsymbol{b}_{GB} = \boldsymbol{b}_1 - \boldsymbol{b}_2$. Because dislocation $\boldsymbol{b}_2$ is strongly attracted to the GB dislocation, the traverse motion of the dislocation through GB is pinned by this attractive force. To surmount the pinning, stress enhancement by a pileup of dislocations is required. Then, many dislocations around the GB interact to form more stable configurations of high-density dislocations. Dislocation walls (small angle GBs) are formed by the rearrangement of dislocations. Misorientation angles of GBs vary by absorbing dislocations [30]. Dislocations are annihilated by dislocation reactions in the grains' interiors, on the GBs, and in the dislocation walls. All these possible processes include the climb motion of dislocations, and the rates of the processes are limited by self-diffusion in grains or in GBs as expressed by eq.(14).

Understanding the nature of GB dislocations is also important for a better understanding of the deformation behavior of polycrystalline ice. Burgers vectors of GB dislocations are different depending on the regularities of the GB; a shorter Burgers vector for more irregular GB. A regular GB can be expressed by a coincidence site lattice (CSL), and possible Burgers vectors of GB dislocations in certain CSLs are predicted by the displacement-shift-complete (DSC) lattice. Several important CSLs and the Burgers vectors of GB dislocations in ice are tabulated in reference [31]. The details are beyond the scope of this review.

4.4 Deformation of polycrystalline ice

As discussed in the preceding sections, ice plasticity is very anisotropic. Therefore, we should pay careful attention to the orientation distribution of crystals included in specimens, or the ice fabrics. From detailed analyses of deformation experiments, Azuma [32] deduced a new strain-rate equation with a dependence on an average Schmidt factor $\overline{S}$. He obtained the fourth power law of $\overline{S}$. He also developed a semi-empirical theory to describe fabric evolution in ice sheets and a tensor notation for the enhancement factor that introduces anisotropy into the flow law of ice sheets [33, 34]. Later, Castelnau et al. [35] developed a more general and rigorous treatment using the viscoplastic self-consistent (VPSC) model. In this section, for better understanding of this rather complicated phenomena, a basic derivation of the fourth power law of $\overline{S}$ is explained following Azuma [32].

When polycrystalline ice is deformed under uniaxial stress σ, the strain rates of individual grains depend on their c-axis orientations with respect to the stress axis. The resolved shear stress τ_i on the basal plane of the i-th grain is $\tau_i = S_i\sigma$, using the Schmidt factor S_i. In addition, we assume that the deformation is only through the shear strain by the basal slip γ_i. Although crystals with larger S_i are preferentially deformed at the beginning of the deformation, as deformation continues crystals with smaller S_i are also deformed to accommodate stress concentrations caused by preferential local deformation. Hence, during steady-state deformation, we assume that every grain is deformed at the same energy-dissipation rate; that is

$$\sigma\dot{\varepsilon} = \tau_i\dot{\gamma}_i \qquad (i = 1, N) \tag{18}.$$

In this context, we also assume that the shear stress τ_i is expressed by $\tau_i = \overline{S}\sigma$, using an average Schmidt factor $\overline{S} = (1/N)\Sigma S_i$. This should be averaged over a small region of the material, but it must include a sufficient number of grains. The shear strain rate of individual grains can be related by a power law to the shear stress as $\dot{\gamma}_i = \beta\tau_i^n$. Then,

$$\dot{\varepsilon} = \beta\overline{S}^{n+1}\sigma^n \tag{19}.$$

Substituting n=3 into eq.(19), we obtain the fourth power law of the average Schmidt factor.

5. Summary

In this review article, the characteristic nature and behavior of dislocations and point defects in ice are described using current dislocation theory. All possible slip systems are discussed, and peculiar deformation modes by nonbasal slips are

described by including the extended dislocations on the basal plane. The kink diffusion model is applied to the mobility of the basal dislocations, and includes recent experimental results obtained by a new x-ray topography method. Applications of dislocation theory to the plastic deformation of ice are also described.

Acknowledgements

I gratefully acknowledge the research staff and Ph. D. students of the Department of Applied Physics and Institute of Low Temperature Science, Hokkaido University for teaching me many things about lattice defects in ice during the discussions we've had over the past two decades.

References

1. A. Fukuda, T. Hondoh and A. Higashi, *J. Phys.*, Paris, 48(3), 163-173 (1987).
2. J.P. Hirth and J. Lothe, *Theory of Dislocations 2nd ed.*, Krieger Publ. Co., pp.857 (1992).
3. T. Hondoh, T. Itoh, S. Amakai, K. Goto and A. Higashi, *J. Phys. Chem.*, 87(21), 4040-4044 (1983).
4. T. Hondoh, T. Itoh and A. Higashi, *Jpn. J. Appl. Phys.*, 20(10), L737-740 (1981).
5. T. Hondoh, *Seppyo* (*J. Jpn. Soc. Snow and Ice*), 51(3), 184-194 (1989).
6. K. Goto, T. Hondoh, and A. Higashi, *Jpn. J. Appl. Phys.*, 25(3), 351-357 (1986).
7. A. Fukuda, *Seppyo* (*J. Jpn. Soc. Snow and Ice*), 47(1), 15-20 (1985).
8. J. Muguruma, *Kinzoku-Gakkai Kaihou* (*Bullet. Jpn. Inst. Metals*), 10(10), 653-666 (1971).
9. T. Hondoh, H. Iwamatsu and S. Mae, *Philos. Mag.*, A62(1), 89-102 (1990).
10. A. Higashi, A. Fukuda, M. Oguro, T. Hondoh, H. Shoji and K. Azuma, *Lattice Defects in Ice Crystals*, Hokkaido Univ. Press, Sapporo, pp.156 (1988).
11. A. Fukuda, private communication.
12. A. Fukuda, *Mechanisms of plastic deformation of ice single crystals, with special references to the study by X-ray diffraction topography. Doctoral Thesis*, Hokkaido University, pp.236, text in Japanese (1975).
13. Y. Wei and J.P. Dempsey, *Philos. Mag.*, A69, 1-10 (1994).
14. J. Muguruma and A. Higashi, *Nature*, 198(4880), 573 (1963).
15. J. Muguruma and A. Higashi, *J. Phys. Soc. Jpn.*, 18(9), 1261-1269 (1963).
16. J. Muguruma, S. Mae and A. Higashi, *Philos. Mag.*, 13(123), 625-629 (1966).
17. S. Mae, *Philos. Mag.*, 18(151), 101-114 (1968).
18. G. Wakahama, In *Physics of Snow and Ice* (ed. H.Oura), The Institute of Low Temperature Science, Sapporo, 291-311 (1967).
19. H. Yamakami, A. Goto, T. Matsuyama, S. Kinpara, P. Pimienta and T. Hondoh, In *Physics and Chemistry of Ice* (ed. N. Maeno and T. Hondoh), Hokkaido Univ. Press, Sapporo, 511-512 (1992).
20. C. Shearwood and R.W. Whitworth, *Philos. Mag.*, A64, 289-302 (1991).
21. Y. Okada, T. Hondoh and S. Mae, *Philos. Mag.*, A79(11), 2853-2868 (1999).
22. T. Hondoh, In *Physics and Chemistry of Ice* (ed. N. Maeno and T. Hondoh), Hokkaido Univ. Press, Sapporo, 481-487 (1992).
23. V. F. Petrenko and R. W. Whitworth, *Physics of Ice*, Oxford Univ. Press, pp.373 (1999).

24. K. Goto, T. Hondoh and A. Higashi, In *Point Defects and Defect Interactions in Metals* (ed. J. Takamura, M. Doyama and M. Kiritani), Univ. Tokyo Press, Tokyo, 174-176 (1982).
25. H. Itoh, K. Kawamura, T. Hondoh and S. Mae, *J. Chem. Phys.*, 105, 2408-2413 (1996).
26. T. Ikeda, H. Fukazawa, S. Mae, L. Pepin, P. Duval, B. Champagnon, V.Ya. Lipenkov and T. Hondoh, *Geophys. Res. Lett.*, 26(1), 91-94 (1999).
27. T. Ikeda, A.N. Salamatin, V.Ya. Lipenkov and T. Hondoh, In *Physics of Ice Core Records* (ed. T. Hondoh), Hokkaido Univ. Press, Sapporo, (2000).
28. P. Duval, M.F. Ashby and I. Anderman, *J. Phys. Chem.*, 87, 4066-4074 (1983)
29. J.P. Poirier, *Plasticity of Crystalline Solids at High Temperatures*, Yokendo, Tokyo, pp.333 (1980).
30. T. Hondoh and A. Higashi, *Nihon Kessyo Gakkaishi* (*J. Phys. Chem.*), 87(21), 4044-4050 (1983).
31. T. Hondoh and A. Higashi, *J. Crystallog. Soc. Jpn.*, 22(3), 270-281 (1980).
32. N. Azuma, *Cold Regions Sci. Tech.*, 23, 137-147 (1995).
33. N. Azuma, *Earth and Planetary Sci. Lett.*, 128, 601-614 (1994).
34. N. Azuma and A. Higashi, *Ann. Glaciol.*, 6, 130-134 (1985).
35. O. Castelnau, H. Shoji, A. Mangeney, H. Milsch, P. Duval, A. Miyamoto, K. Kawado and O. Watanabe, *Earth and Planetary Sci. Lett.*, 154, 307-322 (1998).
36. J. Perez, C. Mai and R. Vassoille, *J. Glaciol.*, 21, 361-374 (1978).
37. X. Hu, K. Jia, F. Liu, I. Baker and D. Black, *Mat. Res. Soc. Symp. Proc.*, 375, 287-292 (1995).
38. S.J. Jones and J.W. Glen, *Philos. Mag.*, 19, 13-24 (1969).
39. L. Arnaud, J. Baruchel, O. Brissaud, S. de LaChapelle, P. Duval, J. Hartwig, T. Hondoh, V.Ya. Lipenkov, J. Ocampo and E. Pernot, In *ESRF Highlights* 1997/1998, 76-77 (1998).
40. A. Higashi, A. Fukuda, T. Hondoh, K. Goto and S. Amakai, In *Dislocations in Solids* (ed. H. Suzuki, T. Ninomiya, K. Sumino and S. Takeuchi), Univ. Tokyo Press, Tokyo, 511-515 (1985).
41. C. Shearwood and R.W. Whitworth, *J. Glaciol.*, 35(120), 281-283 (1989).
42. T. Hondoh, K. Azuma and A. Higashi, *J. Phys.*, Paris, 48(3), 183-187 (1987).
43. Y. Mizuno and N. Hanafusa, *J. Phys.*, Paris, 48(3), 511-517 (1987).
44. S. Kinpara and T. Hondoh, In *Physics and Chemistry of Ice* (ed. N. Maeno and T. Hondoh), Hokkaido Univ. Press, Sapporo, 509-510 (1992).
45. N. Azuma, Y. Wang, Y. Yoshida, H. Narita, T. Hondoh, H. Shoji and O. Watanabe, In *Physics of Ice Core Records* (ed. T. Hondoh), Hokkaido Univ. Press, Sapporo, (2000).
46. R.O. Ramseier, *J. Appl. Phys.*, 38, 2553-2556 (1967).
47. O.E. Mogensen and M. Eldrup, *J. Glaciol.*, 21, 85-99 (1978).